Journal of Materials Chemistry A

ROYAL SOCIETY OF CHEMISTRY

PAPER

View Article Online
View Journal | View Issue

Cite this: J. Mater. Chem. A, 2026, 14, 12896

10.6% Efficient solution-processed Cu_2ZnSnS_4 solar cells *via* cation substitutions and Li doping

Outman El Khouja,[abcd] Yuancai Gong, *[bc] Alex Jimenez-Arguijo, [bc] Ilhame Assahsahi,[ad] Ivan Caño, [bc] Harris Goniotakis, [bc] Oriol Segura-Blanch,[bc] Alejandro Navarro Güell, [bc] Cristian Radu,[a] Lorenzo Calvo-Barrio,[e] Sergio Giraldo, [bc] Marcel Placidi,[bc] Zacharie Jehl Li-Kao,[bc] Aurelian Catalin Galca *[af] and Edgardo Saucedo *[bc]

Copper–zinc–tin–sulfide (Cu_2ZnSnS_4, CZTS) kesterites a promising earth-abundant and non-toxic absorber for next-generation thin-film photovoltaics. However, sulfur-based CZTS solar cells remain limited in performance, largely due to intrinsic defects and interfacial recombination losses. Here, we systematically investigate the impact of solvent chemistry and extrinsic doping and compositional engineering on the quality of solution-processed CZTS absorbers. A comparative study of three solvents, 2-methoxyethanol (MOE), dimethylformamide (DMF), and dimethyl sulfoxide (DMSO) reveals that all yield phase-pure, and compact films due to a robust Cu^{+}–Sn^{4+} molecular precursor system, with MOE producing the most uniform morphology and superior optoelectronic properties. Rather than focusing on pure CZTS, the solvent screening is conducted on Cd-alloyed CZTS (CZCTS), as Cd incorporation substantially alters precursor coordination and crystallization behavior. Building on the optimized processing route, a synergistic compositional strategy combining silver (Ag) – cadmium (Cd) co-alloying with lithium (Li) doping is introduced to suppress cation disorder, passivate grain-boundary defects, and enhance carrier transport. As a result, the optimized he optimized absorber delivers a champion device with a power conversion efficiency of 10.6%, placing it among the highest efficiencies reported for solution-processed, selenium-free CZTS solar cells. These results highlight the critical role of solvent engineering coupled with targeted extrinsic doping in overcoming the long-standing limitations of CZTS photovoltaics and provide a scalable pathway toward environmentally benign thin-film solar technologies.

Received 19th September 2025
Accepted 17th February 2026

DOI: 10.1039/d5ta07702h

rsc.li/materials-a

Introduction

Copper–zinc–tin–sulfide (Cu_2ZnSnS_4, CZTS) kesterite is a promising earth-abundant and non-toxic material for next-generation thin-film solar cells. As a potential alternative to copper indium gallium selenide (CIGS) and cadmium telluride (CdTe), CZTS offers the advantages of being formed by earth-abundant and environmentally friendly elements. Compared to its selenium-rich counterpart (CZTSSe), sulfur-based CZTS has a wider bandgap (~1.5 eV), making it particularly suitable for applications such as tandem photovoltaics, indoor light harvesting, and photoelectrocatalysis.[1–6] While selenium-based kesterite devices have achieved power conversion efficiencies exceeding 15%, largely due to precise phase control and effective doping/alloying strategies in advanced solution processes,[3,7–11] sulfur-based CZTS solar cells progressed more slowly, with reported efficiencies approaching 13%.[2,12,13] This performance gap is primarily attributed to severe bulk and interface recombination driven by deep-level defects, strong band tailing, and electrostatic potential fluctuations inherent to the kesterite structure.[9,14–16]

CZTS absorbers are commonly synthesized using either vacuum-based physical vapor deposition (PVD) or solution-based molecular ink approaches.[1,8,17,18] Gong *et al.*[7] systematically demonstrated that PVD-based growth of kesterite absorbers proceeds through a complex, multi-step grain fusion process, which makes it challenging to achieve uniform phase formation and to suppress Sn-related antisite defects, such as Sn_{Zn}, Cu_{Sn}, and Cu_{Zn} + Sn_{Zn} defect clusters.[7,14,18] These defects introduce bandgap fluctuations and act as efficient Shockley–

[a]National Institute of Materials Physics, Atomistilor 405A, 077125 Magurele, Ilfov, Romania. E-mail: ac_galca@infim.ro
[b]Electronic Engineering Department, Universitat Politècnica de Catalunya (UPC), Photovoltaic Lab – Micro and Nano Technologies Group (MNT), EEBE, Av Eduard Maristany 10-14, Barcelona 08019, Catalonia, Spain. E-mail: yuancai.gong@upc.edu
[c]Barcelona Center for Multiscale Science & Engineering, Universitat Politècnica de Catalunya (UPC), Av Eduard Maristany 10-14, Barcelona 08019, Catalonia, Spain. E-mail: edgardo.saucedo@upc.edu
[d]Ibn Tofail University, Campus Universitaire, 14000 Kenitra, Morocco
[e]Scientific and Technological Centers (CCiTUB), Universitat de Barcelona (UB), Spain
[f]International Center for Advanced Training and Research in Physics, Atomistilor 409, 077125 Magurele, Romania

Read–Hall recombination centers, thereby limiting device performance. In contrast, solution-based molecular ink methods provide greater flexibility in precursor chemistry and reaction pathways, enabling improved control over cation coordination and oxidation states. In particular, stabilizing the Cu^{+} and Sn^{4+} oxidation state during film synthesis has been shown to effectively reduce defect formation and promote the realization of higher-efficiency kesterite solar cells.[18,19]

Within molecular ink processing, solvent choice plays a crucial role in determining precursor coordination, film morphology, and crystallization behavior.[18,20–24] Aprotic solvents such as dimethyl sulfoxide (DMSO) and dimethylformamide (DMF), as well as quasi-protic solvents like 2-methoxyethanol (MOE), are commonly employed.[10,11,25] High-efficiency CZTSSe devices have been fabricated using DMSO-based inks, while Cd-alloyed CZTS solar cells with 12.3% efficiency have also been achieved using similar solvent systems.[26] More recently, MOE-based processing has enabled CZTS devices with efficiencies up to 11.5%.[13] Despite these advances, a systematic comparison of how different solvents influence film quality and device performance in CZTS-based systems remains limited.

Beyond solvent effects, extrinsic strategies such as cation alloying and alkali doping have proven effective in mitigating intrinsic disorder and improving optoelectronic properties in kesterite absorbers.[27,28] Cd incorporation can suppress secondary phase formation, reduce band tailing, and enhance minority carrier lifetime by mitigating I_{II} (Cu_{Zn}) and IV_{II} (Sn_{Zn}) antisite defects.[29–31] Ag alloying at low concentrations (<10%) has been shown to promote grain growth and reduce Cu_{Zn} disorder,[8,32] while light alkali elements such as Li have demonstrated benefits including increased carrier concentration, grain-boundary passivation, and defect mitigation.[32,33] However, most previous studies have explored these approaches individually, and their combined effects, particularly in sulfur-based CZTS remain insufficiently understood.

Importantly, Cd incorporation substantially alters the coordination environment of metal–thiolate precursors and affects nucleation and crystallization pathways. For this reason, solvent effects in the present study are evaluated directly on Cd-alloyed CZTS (CZCTS) rather than on pure CZTS. While the solvent behavior of pure CZTS has been widely reported in earlier literature, the Cd-containing system requires direct investigation due to its distinct precursor chemistry and crystallization dynamics.

Unlike prior CZTS studies that typically investigate Ag alloying, Cd substitution, or alkali doping as isolated strategies, the present work integrates Ag–Cd co-alloying with Li doping in a pure-sulfide CZTS system using a single, solution-processed molecular ink route. Previous reports have focused either on Ag or Cd alloying without alkali doping, or on Li incorporation in selenide-based CZTSSe absorbers, where the defect chemistry and interface energetics differ substantially from those of sulfide-only CZTS. Here, Ag is employed to suppress Cu–Zn disorder, Cd to tune band alignment and mitigate secondary phases, and Li to passivate grain-boundary and bulk defects. By combining these effects within a controlled precursor chemistry, this work establishes a synergistic defect-management strategy that directly targets the dominant recombination pathways in sulfur-based CZTS.

In this work, we present a comparative evaluation of three solvents: MOE, DMF, and DMSO, used in the preparation of CZTS absorbers. All three solvent systems yield compact, secondary-phase-free films due to a shared Cu^{+}–Sn^{4+} precursor chemistry, highlighting the robustness of the molecular ink formulation. Among them, 2-methoxyethanol (MOE) produces the most uniform and pinhole-free absorber layers, leading to enhanced optoelectronic properties. Furthermore, we report for the first time a co-alloying strategy incorporating Ag and Cd, together with Li doping through a tailored precursor design. This integrated approach of solvent engineering, isoelectronic co-alloying, and alkali doping enables improved film crystallinity, defect suppression, and carrier transport. As a result, high-performance CZTS solar cells are achieved with a power conversion efficiency of 10.6%, featuring an open-circuit voltage (V_{oc}) of 663 mV, a short-circuit current density (J_{sc}) of 23.86 mA cm^{-2}, and a fill factor (FF) of 66.9%. These findings provide new insights into synergistic defect control in sulfide CZTS and demonstrate a viable pathway toward efficient, scalable, and environmentally benign thin-film photovoltaic technologies.

Results and discussion

Fig. 1a shows the structural characterization of Cd-alloyed kesterite $Cu_2(Zn, Cd)SnS_4$(CZCTS) films with a Cd/(Zn + Cd) ratio of 20%, synthesized *via* a molecular ink process using various solvents and sulfurized at 680 °C. A compositional series of Cd substitution (0–30%) was systematically investigated through device performance comparison to determine the optimal alloying level, as detailed in the Fig. S1 and Table S1. Films prepared from three different solvents (DMSO, DMF, and MOE) exhibit sharp diffraction peaks consistent with the tetragonal CZTS phase (ICDD PDF No. 04-015-7542), including dominant diffraction from the (112), (220), and (312) planes at 28.4°, 32.92°, and 47.13°, respectively. The weak shoulder visible near the 112 peak is a typical Cu $K\alpha_1/K\alpha_2$ doublet artifact combined with mild 112/220 texture overlap, commonly observed in oriented kesterite films. Its position does not correspond to any CdS reflection, and the Raman spectra in Fig. 1b show no CdS signal near 302 cm^{-1}, confirming the absence of CdS. The Mo 110 peak at 40.5° (ICDD PDF No. 00-004-0809) confirms substrate integrity post-sulfurization. Critically, solvent variation induces no measurable differences in peak positions, intensities, or full-width-at-half-maximum (FWHM) values as shown in Fig. 1a. This demonstrates that precursor chemistry, unlike conventional solvent-dependent nanoparticle synthesis methods, has a negligible influence on crystallite size, phase purity, or preferential orientation.[25,34] Because this study aims to optimize the Cd-alloyed absorber, the solvent comparison is performed directly on CZCTS. Pure CZTS solvent trends have been extensively reported in earlier literature and are used as established references. Focusing on CZCTS avoids duplicating known CZTS results and provides a more meaningful evaluation of solvent–Cd precursor interactions.

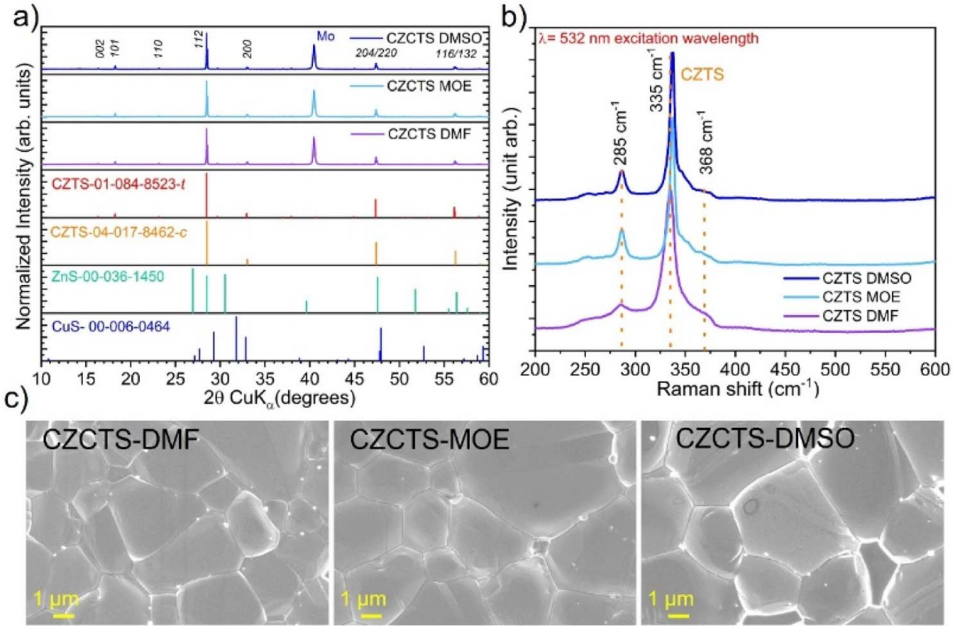

Fig. 1 (a) X-ray diffraction, (b) Raman spectroscopy, (c) top-view SEM images of CZCTS films elaborated using different solvents.

The solvent-agnostic structural consistency highlights the robustness of the precursor design, ensuring uniform phase evolution and secondary phase-free crystallization during thermal processing.[18,21] The high crystallinity (evidenced by narrow FWHM, Fig. 1a) and presumably absence of secondary phases (*e.g.* CuS, ZnS, Cu_2SnS_3) further highlight the method's capacity to decouple solvent selection from the optoelectronic properties of the film. Such reproducibility across solvent systems positions this approach as a versatile platform for scalable, solution-processed kesterite films, where solvent adaptability can be leveraged for ink engineering, such as tuning viscosity or deposition kinetics, without significantly changing the phase quality and purity. Furthermore, Raman spectroscopy (532 nm excitation wavelength, Fig. 1b) probes the phase composition, defect states, and cation sulfur bonding dynamics in CZTS, revealing vibrational modes critical to its optoelectronic functionality.

The three absorber films show similar Raman spectra with the characteristic peaks of CZTS at around 285 cm^{-1} (B mode B_{285}), 335 cm^{-1} (A mode A_{335}), and 368 cm^{-1} (B mode B_{354}), corresponding to distinct cation-sulfur vibrational alignments.[35,36] The absence of other relevant features suggests low concentration or even absence of secondary phases, as well as similar crystallinity quality, in agreement with XRD (Fig. 1a).

The scanning electron microscope (SEM) analysis (Fig. 1c) reveals how solvent selection governs morphological evolution without perturbing the phase purity or defect chemistry resolved above. DMSO-processed films exhibit large grains (≈8 μm) (Fig. S2) and low porosity, attributed to slow evaporation, which enables adatom diffusion, consistent with the narrow Raman peak widths (FWHM ≈ 12 cm^{-1}) signaling low lattice disorder. MOE-derived films show intermediate grain sizes (≈6 μm) and smooth surfaces, reflecting balanced evaporation kinetics that suppress potential secondary phase segregation while enabling moderate crystallite growth. In contrast, DMF's slower evaporation due to its higher boiling point results in smaller grains (≈5 μm) and higher roughness, yet the XRD pattern and Raman spectra confirm retained crystalline quality, underscoring the precursor design's resilience to solvent-driven kinetic variations. This decoupling of morphology (governed by solvent kinetics) from structural/defect properties (locked by precursor chemistry) enables tunable ink processability without sacrificing electronic quality, which is an important advantage for scalable, solution-processed kesterite photovoltaics.

Current density–voltage (J–V) analysis reveals how solvent-driven morphological variations (Fig. 2a) govern the electronic performance of solution-processed CZTS solar cells. Devices fabricated with DMF exhibit a moderate open-circuit voltage (V_{oc} = 610 mV) and a short-circuit current density (J_{sc} = 22.14 mA cm^{-2}), but a low fill factor (FF = 46.79%) limits their power conversion efficiency (PCE = 6.32%). The increased J_{sc} aligns with DMF's porous, small-grained morphology (Fig. 1c), which enhances light scattering and carrier generation. However, the suppressed FF reflects resistive losses, likely originating from grain boundary scattering and suboptimal percolation pathways for charge transport, consistent with the film's roughness and discontinuous microstructure. This tradeoff indicates the interplay between optical absorption (associated with increased porosity or surface roughness) and degraded charge transport (due to structural inhomogeneity). In contrast, the DMSO-processed device exhibits a higher V_{oc} (630 mV) and FF (51.24%), suggesting improved suppression of bulk and/or grain boundary recombination. This improvement is likely to be due to the formation of larger grains and enhanced defect properties, as confirmed by the reduced

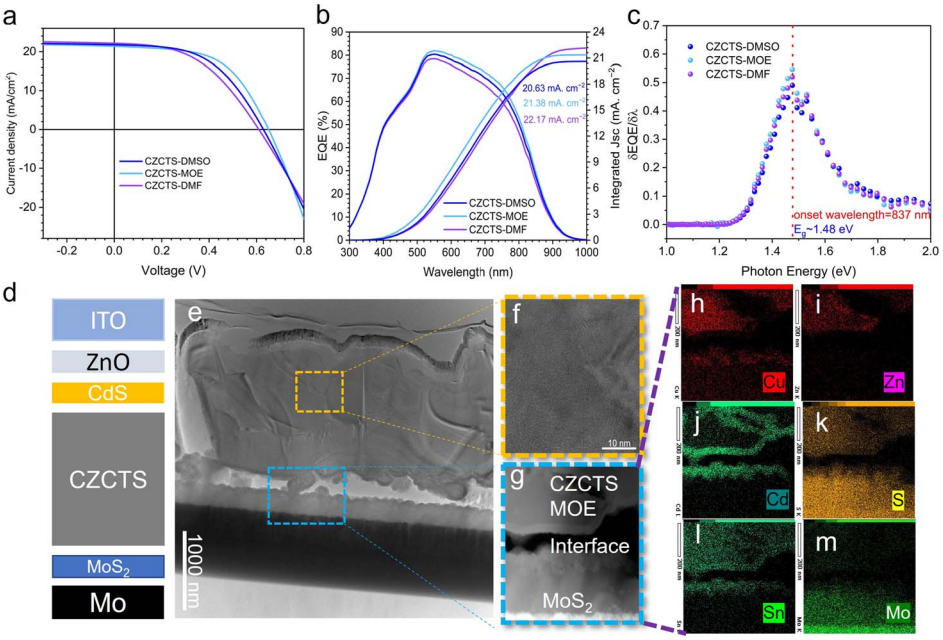

Fig. 2 (a) J–V characteristics of the device based on the absorber elaborated using different solvents (b) EQE spectra of these same cells, and the integrated J_{sc} derived from the EQE spectrum is in good agreement with the J–V extracted value (deviation < 3%). (c) Plot of first derivative of EQE *versus* photon energy for CZCTS solar cells, (d) device architecture (e–g) bright-field TEM image of cross-sectional CZCTS MOE, cross-sectional STEM image of a region near the CdS/CZCTS heterointerface, (h–m) EDS mappings of the CZCTS MOE device.

Urbach energy (SI, Fig. S2). However, the slight observed reduction in J_{sc} (21.76 mA cm^{-2}) may arise from several contributing factors, such as macroscopic inhomogeneity, interfacial recombination, or potential band misalignment at the Mo/CZTS interface. Devices derived from MOE outperform both alternatives, achieving the highest V_{oc} (646 mV), J_{sc} (21.84 mA cm^{-2}), FF (56.01%), and PCE (7.91%). The decent performance stems from MOE's intermediate evaporation kinetics, which yield smooth, defect-suppressed films with optimal grain connectivity. The enhanced V_{oc} arises from reduced non-radiative recombination, as evidenced by the narrowed Raman A_{335} peak intensity (Fig. 1), indicating a low concentration of Cu–Zn antisite defects. Concurrently, the high J_{sc} reflects improved carrier collection efficiency due to longer minority-carrier diffusion lengths, enabled by the film's uniform crystallite size and low intra-grain disorder.

The FF, though limited by series resistance from the potential C residual from MOE ligands, is enhanced by the improved absorber quality, which promotes a stronger built-in electric field and a lower-defect heterojunction interface. External quantum efficiency (EQE) spectra (Fig. 2b) confirm strong broadband absorption (peak ~75% at 550–650 nm), with derivative analysis (Fig. 2c) pinpointing a bandgap ($E_g \approx 1.48$ eV) near the Shockley–Queisser optimum for single-junction devices. The short-circuit current densities calculated by integrating the EQE spectra under AM 1.5G illumination are consistent with the corresponding J–V extracted J_{sc} values, with deviations below ±3%, confirming the reliability of the photovoltaic characterization. The low Urbach tail in MOE/DMSO films (Fig. S3) aligns with their expected low mid-gap defect densities, consistent with possible suppression of non-radiative recombination and higher V_{oc}. These improvements arise from enhanced grain connectivity and optimized interface quality, modulated by solvent kinetics, while maintaining phase purity confirmed by XRD and Raman analysis. This work demonstrates that solvent engineering can decouple morphological control from defect formation, providing a robust strategy for tuning ink formulations without compromising the phase quality and electronic performance. These insights advance solution-processed chalcogenides toward scale-up feasibility by linking morphological control to defect suppression and charge extraction efficiency.

The performance of kesterite-based solar cells is critically influenced by interfacial properties, which determine charge extraction and recombination dynamics. Cross-sectional electron microscopy and elemental mapping (Fig. 2d, panels e–n) reveal key structural and chemical features of the CZCTS/CdS and CZCTS/MoS_2 heterojunctions, which are the most critical interfaces in these devices. High-resolution TEM (Fig. 2e–g) demonstrates a well-defined multilayer structure (ITO/ZnO/CdS/CZCTS/MoS_2/Mo), with a clearly defined CZCTS/CdS interface and a discontinuous CZCTS/MoS_2 interface, as observed in STEM-HAADF imaging (Fig. 2e).

However, elemental maps (panels h–n) indicate consistent Mo and S signals at the back-contact region, associated with the spontaneous formation of a MoS_2 interlayer during sulfurization. Although MoS_2 is widely regarded to enhance charge extraction and transport by optimizing band alignment from a Schottky-type to an Ohmic-type contact (consistent with the improved $V_{oc} = 635$ mV in DMSO-processed devices, Fig. 2a), its

thickness and phase purity are critical factors for minimizing resistive losses. Fig. 2f presents clear micrographs with well-defined lattice plane patterns, indicating the high crystalline quality of the film. The Zn and S maps (Fig. 2h–m) further suggest stoichiometric deviations near grain boundaries, likely contributing to mid-gap defect states that limit carrier lifetimes. These findings align with the limited EQE (Fig. 2b) and high band tail states ($E_u \sim 45$ meV, Fig. S3) observed in devices with excessive interfacial disorder. To mitigate these losses, controlled sulfurization processes are proposed to refine the MoS_2 thickness and suppress deleterious elemental interdiffusion. For instance, tuning sulfur partial pressure during annealing could stabilize a phase-pure, ultrathin MoS_2 layer (<5 nm), leveraging its favorable band alignment with CZCTS. Such interfacial engineering, coupled with the defect-suppressed morphologies achieved in MOE-derived absorbers (Fig. 2d, panels e–g), offers a pathway to reconcile high V_{oc} (>640 mV) and J_{sc} (>21 mA cm^{-2}) in solution-processed kesterites, as proved in Fig. 2a.

Further insights from high-resolution TEM (HRTEM) and elemental EDS mapping confirm structural and compositional uniformity across the CZCTS/MoS_2 interface. The CZCTS layer exhibits homogeneous contrast with no visible secondary phase segregation at the back contact region, suggesting a stable single-phase absorber. Elemental distribution maps reveal a uniform dispersion of Cu, Zn, Sn, and S throughout the bulk, while Cd predominantly appears around grain boundaries. This indicates that the CdS bath infiltrates the absorber through surface holes, resulting in the deposition of CdS at the back interface during the chemical bath deposition (CBD) process. This Cd-enrichment at grain peripheries likely contributes to improved surface passivation and reduced interfacial recombination. Moreover, the absence of Mo-rich clusters or discontinuities in the MoS_2 layer supports its role as a conformal back-contact interlayer. Collectively, these microstructural observations further validate the effectiveness of the optimized sulfurization and processing strategies in achieving high-performance, defect-tolerant CZCTS absorbers.

Furthermore, Ag and Li were added to the precursor solution at ratios of Ag/(Cu + Ag) = 10% and Li/(Ag + Cu) = 2 or 4%, respectively, to further enhance absorber quality and mitigate detrimental intrinsic defects.

Previous studies have demonstrated that the synergistic effect of cation substitution and light alkali doping can significantly boost Se-rich CZTSSe device performance.[32] Structural and morphological analyses reveal how Ag alloying and Li doping affect CZCTS thin films. Energy-dispersive X-ray spectroscopy (EDX) was employed to examine the elemental composition of CZCTS and Ag-alloyed CZCTS (ACZCTS) films in both the as-deposited and sulfurized states (Fig. S4 and Table S2). The measured elemental ratios remain close to the nominal precursor compositions after sulfurization, indicating negligible cation loss or segregation during high-temperature processing. Importantly, Ag incorporation does not induce measurable deviations in the overall Cu–Zn–Sn–Cd stoichiometry, confirming that Ag is introduced in a controlled manner without disrupting the kesterite lattice chemistry. These results demonstrate that the sulfurization process preserves compositional integrity and that the structural and photovoltaic improvements observed upon Ag and subsequent Li incorporation arise from intentional defect and lattice engineering rather than unintended stoichiometric fluctuations. Given the semi-quantitative nature of EDX, the analysis is used here to verify compositional stability rather than absolute stoichiometry, which is sufficient to support the conclusions drawn in this study. In addition, EDX elemental mapping of the as-deposited CZCTS and ACZCTS precursor films (Fig. S4) shows a homogeneous spatial distribution of all constituent elements, indicating uniform precursor mixing prior to sulfurization.

X-ray photoelectron spectroscopy (XPS) was employed to further examine the surface composition and chemical states of the CZCTS and Li-doped ACZCTS absorber layers. The corresponding XPS survey and high-resolution core-level spectra (Cu 2p, Zn 2p, Sn 3d, Cd 3d, Ag 3d, and S 2p) are provided in Fig. S5, confirming the presence of all constituent elements with binding energies consistent with kesterite CZTS. Lithium is not directly detected by XPS, which is expected due to its low atomic concentration, weak photoionization cross-section, and its tendency to reside at grain boundaries or interfaces rather than forming a distinct bulk chemical environment. Together with the EDX results obtained for both as-deposited and sulfurized films (Fig. S4 and Table S1), these analyses confirm the compositional integrity and stability of the absorber layers.

XRD patterns match the kesterite phase of CZTS, aligning with the reference pattern ICDD PDF No. 01-084-8523. The small shoulder near the 112 reflection originates from the Cu Kα doublet and minor texture effects; its position does not match any CdS 002 or 101 reflection. This interpretation is supported by the Raman spectra in Fig. 3b, which show no CdS feature at 302 cm^{-1}, confirming single-phase kesterite across all compositions. Ag doping (10%, labeled as "10%Ag–0%Li" in Fig. 3a) induces slight peak shifts, without forming new phases, indicating successful substitution of Cu by Ag in the lattice. Subsequent Li doping (2% and 4%, labeled "10%Ag–2%Li" and "10%Ag–4%Li" in the figure) does not result in any visible additional peak shifts, suggesting that Li incorporation causes only minimal lattice distortion or occurs without significantly altering the crystal structure. Ag incorporation appears to influence Raman spectral features, with possible variations in peak intensities that may suggest changes in crystallinity or local structural order. Increasing Li concentrations (2% and 4%), peak broadening, and slight shifts are observed particularly around 334 cm^{-1} and 367 cm^{-1} (highlighted in the inset of Fig. 3b), reflecting an increase of structural disorder, consistent with local lattice distortions or defect clustering. Such behavior aligns with prior observations reported by Dimitrievska *et al.*[36] where Raman broadening in kesterite phases was correlated with increased cation disorder and compositional inhomogeneity. SEM images (panel c, labeled by composition) highlight doping-induced morphological changes. Undoped CZCTS ("0% Ag–0%Li") exhibits large, well-defined grains (visible in gray-scale images with textured surfaces). Ag alloying produces a denser, smoother morphology with reduced grain boundaries (*e.g.*, "10%Ag–0%Li" in the grid), suggesting improved

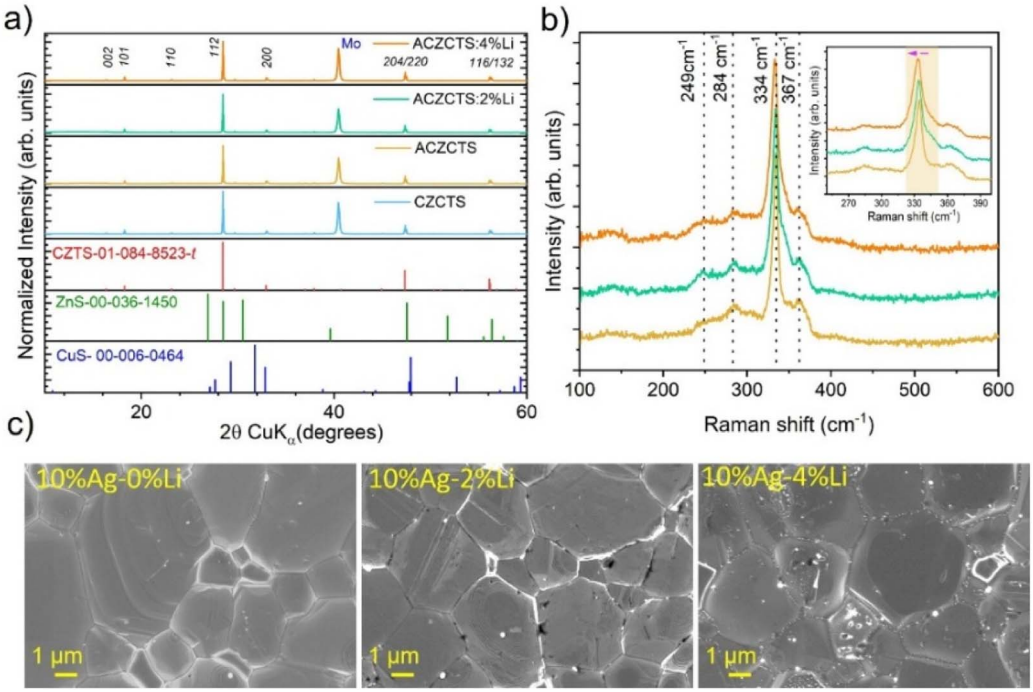

Fig. 3 (a) X-ray diffraction, (b) Raman spectroscopy, (c) top-view SEM images of CZCTS MOE-doped and undoped Li films.

crystallization. Li co-doping (2% and 4%) leads to small surface particles (visible as bright spots in "10%Ag–4%Li" images) and irregular grains, becoming more pronounced at higher Li concentrations. Cross-section micrographs (Fig. S6) show dense film growth, with surface particles likely linked to phase segregation.

These particulates are probably related to residual lithium-containing phases, such as LiCl (formed *via* decomposition of $LiClO_4$) or Li_2S, which can emerge during the sulfurization process. Such Li-rich species are known to function as flux agents, promoting grain coalescence and enhanced crystallinity during high-temperature treatments. However, these Li-based residues exhibit high solubility in the chemical bath deposition (CBD) solution used for CdS growth and are therefore expected to be removed during the CdS deposition process. As a result, they are unlikely to persist in the final device stack or adversely affect photovoltaic performance.[32,37]

The sequential modifications applied in this work, solvent selection, Cd substitution, Ag alloying, and Li doping, each target distinct defect populations and electronic bottlenecks. Ag reduces Cu–Zn disorder, Cd tunes surface stoichiometry and conduction-band alignment, and Li passivates grain-boundary states while modulating carrier density. The combined effect produces measurable improvements in TRPL lifetime, ideality factor, and *J–V* characteristics. The strategic incorporation of Ag and Li dopants into CZCTS yields significant performance enhancements through systematic defect engineering, as demonstrated by structural and optoelectrical behavior provided in Fig. 4a.

The baseline CZCTS device exhibited a PCE of 7.91%, characterized by V_{oc} = 646 mV, J_{sc} = 21.84 mA cm^{-2}, and FF = 56.05%, limited by intrinsic defects such as Cu_{Zn} antisite disorders and grain boundary recombination. Substituting 10% Ag to form $Ag_{0.1}Cu_{1.9}Zn_{0.8}Cd_{0.2}SnS_4$ (ACZCTS) resulted in an improved PCE of 8.5%, with corresponding increases in V_{oc} to 679 mV and J_{sc} to 22.41 mA cm^{-2} attributed to mitigating Cu_{Zn} antisite defects and enhanced band alignment, as Ag substitution typically reduces cation disorder in the kesterite lattice, as evidenced by XRD analysis showing sharper 112 and 220/204 peaks (Fig. 3). The sharper diffraction peaks indicate improved crystallinity, while the absence of secondary phases in XRD and Raman spectra (Fig. 3) confirms phase purity, with the Ag-doped sample exhibiting a slight shift in the dominant A1 Raman mode (338 cm^{-1}), suggesting lattice strain modulation.

The subsequent introduction of Li as a dopant in the ACZCTS system revealed an optimal concentration window for performance enhancement. At 2% Li doping, the ACZCTS device achieved peak performance with a PCE of 9.05%, J_{sc} of 24.23 mA cm^{-2}, V_{oc} of 679 mV, and FF of 55.01% (Fig. 4a). The enhanced performance correlates with two key microstructural improvements. Firstly, the development of well-oriented columnar grains, as evidenced by cross-sectional SEM analysis (Fig. S6), suggests reduced grain boundary recombination, and on the other hand, enhanced EQE spectral response in the 500–700 nm region, reflecting improved charge carrier collection efficiency and reduced bulk recombination (Fig. 4b). The EQE spectrum also shows a sharp absorption onset, indicating that the optical band gap remains unchanged, indicating that the fundamental electronic structure of the ACZCTS absorber is preserved, which suggests that the PCE improvement is primarily driven by defect passivation rather than modification to the bulk band structure. Integration of the EQE spectra

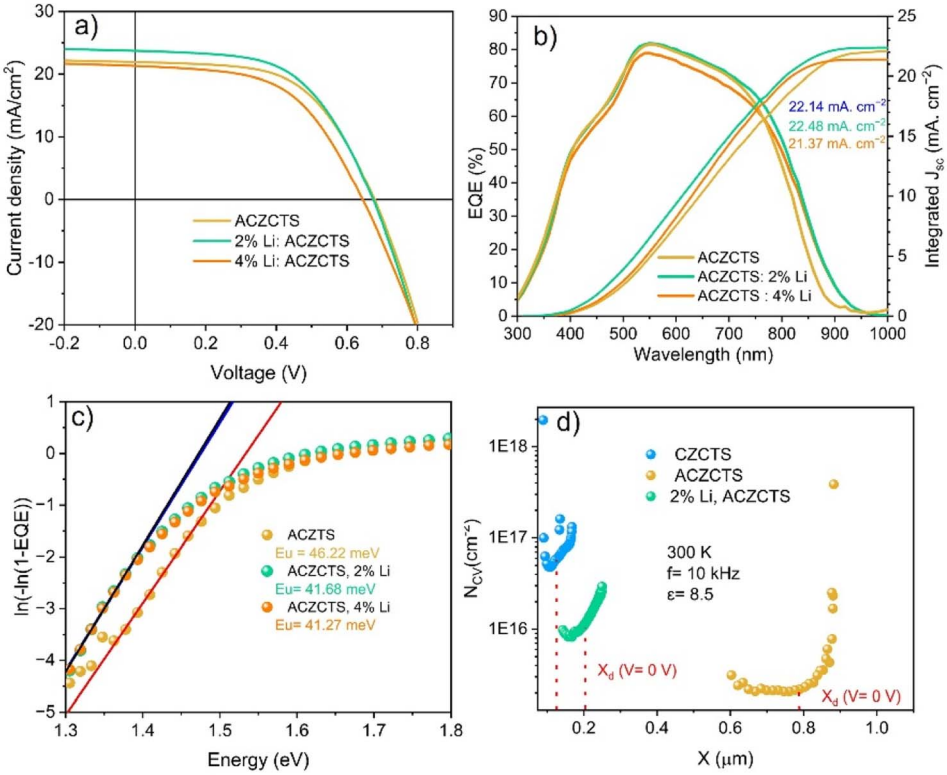

Fig. 4 (a) J–V curves, (b) EQE spectra and the EQE-integrated J_{sc} is matching the J–V measured J_{sc} within experimental uncertainty (±3%), (c) Urbach energy calculation of the devices fabricated based on Li doped and undoped ACZCTS MOE devices, (d) carrier density profiles extracted by C–V analysis.

confirms that the resulting J_{sc} values closely match those obtained from J–V measurements, with discrepancies remaining within ±5%, indicating that the observed performance enhancement originates from improved carrier collection rather than measurement artefacts. Importantly, the Urbach energy derived from the EQE absorption edge exhibits minimal change, supporting the conclusion that band tailing due to disorder or defect-induced localized states has been effectively reduced or suppressed (Fig. 4c). This reduction in sub-bandgap absorption is consistent with the minimization of shallow defects, which are often associated with broadened absorption tails.

Li is likely incorporated as Li_{Cu} or Li_{Zn} antisites or interstitials, which are known to passivate deep-level defects and improve the p-type conductivity.[32,37] This defect passivation reduces carrier recombination, leading to enhanced J_{sc}, V_{oc}, and FF. In addition, the unchanged bandgap and improved EQE suggest reduced parasitic optical losses and shadowing defects, particularly at the front interface. Carrier loss arising from incomplete coverage, voids, or non-uniformities in the buffer or TCO layers can limit spectral response. Their suppression through the optimized Li doping process results in more uniform light absorption, efficient carrier generation, and enhanced collection, further corroborated by the low Urbach energy and sharp EQE onset. However, increasing Li concentration to 4% resulted in performance deterioration with PCE of 7.55%, J_{sc} = 21.77 mA cm^{-2}, V_{oc} = 649 mV, and FF = 53.50%, suggesting a critical doping threshold beyond which detrimental effects dominate. This degradation likely stems from the formation of secondary phases at grain boundaries, increased carrier compensation from defect clustering, or the introduction of deep-level defects that act as recombination centers.[38]

Structural characterization provides insight into the impact of higher Li concentrations on phase stability. No additional crystalline secondary phases are detected for the 4% Li-doped samples within the resolution limits of XRD and Raman spectroscopy, indicating that excess Li does not segregate into bulk crystalline compounds. However, Raman spectra exhibit noticeable peak broadening and reduced intensity at higher Li concentration, which points to increased local structural disorder rather than the formation of a new crystalline phase. This behavior suggests that excessive Li preferentially accumulates at grain boundaries or interfaces, where it can form Li-rich, highly disordered or amorphous regions that are not readily detectable by conventional structural probes. Such local segregation is expected to promote defect clustering and carrier compensation, thereby introducing recombination-active centers that degrade V_{oc}, FF, and overall device performance.

From a spectroscopic standpoint, the defect-passivation role of Li incorporation is consistently supported by multiple independent measurements. The reduced Urbach energy extracted from the EQE absorption edge indicates a suppression of band-tail states associated with disorder-induced defect clusters. This trend is accompanied by an enhancement in carrier lifetime

observed in time-resolved photoluminescence measurements and a reduction in the density of electrically active trap states inferred from admittance and *C–V* analysis. Importantly, no measurable shift in the optical bandgap is observed upon Li incorporation, confirming that the performance enhancement originates from defect mitigation rather than band-structure modification. Together, these complementary spectroscopic signatures demonstrate that Li primarily passivates recombination-active bulk and grain-boundary defects, thereby suppressing non-radiative recombination and improving carrier collection in the optimized ACZCTS absorber.

The synergistic effects of Ag and Li co-doping highlight the importance of defect engineering in kesterite solar cells. The optimal performance achieved with 2% Li:ACZCTS represents a balance between beneficial grain growth promotion, defect passivation, and the onset of deteriorative effects at higher doping concentrations (Fig. 4c). (Fig. 4d) shows the apparent carrier concentration profiles, extracted from capacitance–voltage (*C–V*) measurements at 300 K (10 kHz), for pure CZCTS, Ag-alloyed CZCTS (ACZCTS), and 2% Li-doped ACZCTS (Li:ACZCTS) films. The depletion width at zero bias (X_d, $V = 0$ V) is indicated. The pure CZCTS film exhibits the highest carrier density ($\sim 10^{17}$ cm^{-3}), consistent with a high concentration of intrinsic acceptor defects (*e.g.*, Cu_{Zn} antisites and Cu vacancies) typical of kesterite structures. Alloying with 10% Ag (ACZCTS) leads to a pronounced reduction in carrier density ($\sim 10^{15}$ cm^{-3}) and an expanded depletion region ($\sim$0.8 μm).

This is attributed to the suppression of intrinsic defect formation, as Ag^+ substitution for Cu^+ reduces antisite defect densities, in line with previous reports on Ag-alloyed kesterites. Upon introducing 2% Li into the ACZCTS absorber, a moderate increase in carrier concentration is observed from ($\sim 10^{15}$ cm^{-3}) (minimum in the profile) to ($\sim 10^{16}$ cm^{-3}) along with a corresponding decrease in depletion width. This suggests that Li acts as a shallow donor or modulates the defect equilibrium, partially compensating for acceptor defects and thereby enhancing the free carrier density. Such tuning of the doping level can help balance carrier transport and junction properties, supporting improved device performance.

A 2% Li doping in ACZCTS significantly improves efficiency and reproducibility, as indicated by statistical analysis of device performance (Fig. 5). In addition to showing significantly less variance in V_{oc} (ΔIQR > 40%) and J_{sc}, the 2% Li:ACZCTS devices outperform pure CZCTS (median: 7.8%) and undoped ACZCTS (median: 8.4%) with a median PCE of 9.05% (8.8–9.3%). According to EQE and Urbach energy analysis, this homogeneity results from Li-induced passivation of deep-level defects (Cu_{Zn} antisites, Sn_{Zn}, and related clusters), which reduces carrier recombination and permits well-oriented columnar grain growth. Crucially, performance deterioration (PCE = 7.55%) and increased dispersion are likely caused by defect clustering and secondary phase formation when the 2% Li threshold is exceeded (*e.g.*, 4% Li samples). Defect suppression and harmful doping are thus delicately balanced by the optimized co-doping strategy. Further introduction of 2% Li (Li:ACZCTS) results in a modest increase in carrier concentration compared to ACZCTS, while maintaining a relatively wide depletion region.

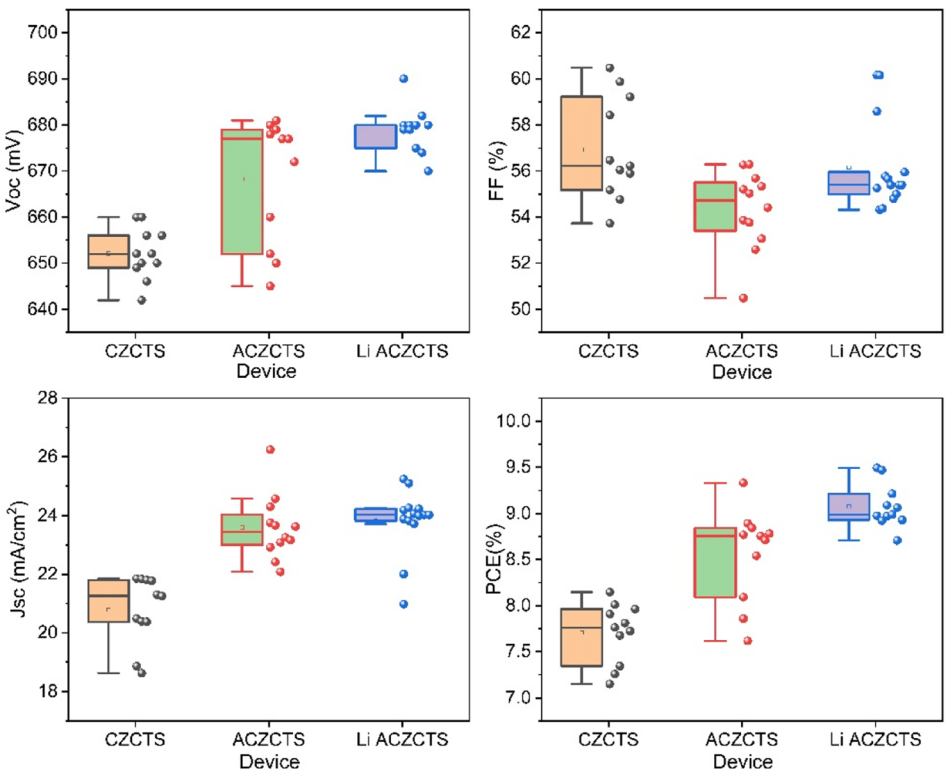

Fig. 5 Statistical distribution of the photovoltaic parameters for the devices based on CZCTS, ACZCTS, and 2% Li ACZCTS films.

The Li dopants likely passivate residual compensating defects or modulate the defect chemistry, partially restoring free hole density without significantly degrading junction quality. Together, these trends demonstrate that targeted Ag alloying and controlled Li doping effectively tailor the electrical properties of CZCTS absorbers by modulating the defect landscape, providing key avenues for optimizing device performance. Further optimization of precursor conditions and annealing atmosphere enabled the fabrication of a champion device based on the same 2% Li:ACZCTS composition, achieving a PCE of 10.6%, J_{sc} of 23.86 mA cm^{-2}, V_{oc} of 663 mV, FF of 66.9%. Based on repeated measurements of multiple devices fabricated under identical conditions, the uncertainty in the extracted photovoltaic parameters is estimated to be within ±1% for PCE, ±10 mV for V_{oc}, ±0.6 mA cm^{-2} for J_{sc}, and ±2% for fill factor, indicating that the champion device performance is representative of the reproducible device distribution.

The corresponding EQE spectrum exhibits a peak with a spectral response of up to 86%, confirming effective photocarrier generation and collection across a broad spectrum. This champion device performance, included in (Fig. 6a and b), underscores the reproducibility and scalability of the Li/Ag co-alloying approach. The short-circuit current density obtained by integrating the EQE spectrum is in good agreement with the *J–V* extracted J_{sc} of the champion device, further validating the accuracy of the reported photovoltaic parameters. The reported champion efficiency of 10.6% represents the upper bound of a reproducible device distribution obtained from more than 20 devices fabricated under identical conditions. Across this device set, the standard deviation of the extracted *J–V* parameters (V_{oc}, J_{sc}, FF, and PCE) remains within the reported uncertainty ranges, while repeated EQE measurements exhibit negligible spectral variation, with EQE-integrated J_{sc} values varying by less than ±3–5%, confirming the statistical reliability of the presented *J–V* and EQE results. In addition to reproducibility, device stability was evaluated by re-measuring the *J–V* characteristics of the champion Li:ACZCTS device after 500 h storage under ambient laboratory conditions. As shown in Fig. S7, the device retains most of its initial photovoltaic performance, with no significant changes in V_{oc}, J_{sc}, or fill factor, indicating reasonable short-term performance durability of the optimized absorber and device architecture.

Beyond bulk defect passivation, statistical reproducibility, and performance stability, the V_{oc} is strongly influenced by recombination at both the back and front interfaces of the device. On the back-contact side, sulfurization conditions were carefully optimized to promote the formation of a thin and continuous MoS_2 interfacial layer, which is known to improve band alignment at the Mo/CZTS interface while minimizing interface recombination. Excessive MoS_2 growth, which can increase series resistance and act as a recombination pathway, was avoided by controlling the sulfur partial pressure and annealing duration. At the front interface, the CdS buffer layer was deposited using a controlled chemical bath deposition process. The improved absorber surface quality achieved through Ag–Cd alloying and Li-induced defect passivation reduces the density of interface states at the CZTS/CdS junction, thereby suppressing interface-assisted recombination. These interfaces optimizations contribute to the enhanced V_{oc} observed in the optimized devices; however, the remaining V_{oc} deficit is attributed to residual band-tail states and intrinsic interface recombination in sulfide CZTS, indicating that further interface engineering will be required to approach the radiative limit.

The observed enhancement reflects the synergy between microstructural refinement (Fig. 6c) and electronic improvements, particularly through the suppression of recombination-active defects and improved carrier collection across the absorber thickness. The presented results offer a concrete pathway for advancing performance limits in kesterite photovoltaics through defect-targeted alloying strategies. Further work should aim to elucidate the mechanistic role of Li incorporation, its spatial distribution, interaction with Ag, and influence on local defect chemistry and band alignment. Expanding this approach to include alternative co-dopants and post-deposition passivation treatments may unlock additional gains in efficiency, stability, and reproducibility.

A comparison of our CZTS solar cell's photovoltaic performance with the top devices in recent research is shown in Table 1. The present work explores the combined influence of Li doping with dual cation alloying (Cd and Ag) in a pure-sulfide CZTS absorber, providing complementary control over defect passivation and charge transport. The champion device reaches a PCE of 10.6%, placing it among the highest efficiencies

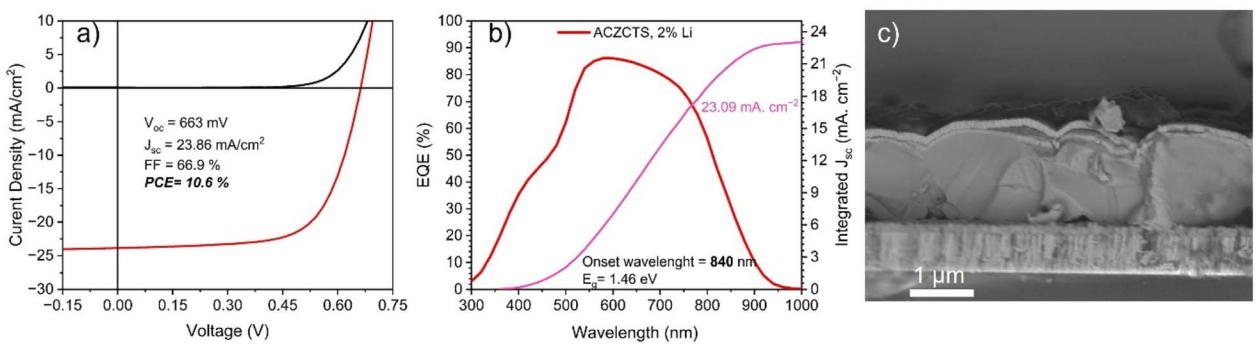

Fig. 6 (a) *I–V* curve, (b) EQE spectra and the integrated J_{sc} obtained from EQE is consistent with the *J–V* extracted current density of the champion device, and (c) cross-section SEM image of the champion devices made with 2% Li doping ACZCTS.

Table 1 Photovoltaic parameters of representative high-performing CZTS-based solar cells reported in the literature, compared with the champion device from this work. The comparison highlights different compositional and recombination–transport trade-offs rather than a direct ranking of device performance. For this work, diode parameters are reported for the champion Li:ACZCTS device to illustrate the balance between transport and recombination achieved through Li doping combined with Ag–Cd alloying

Alloying	Doping	PCE (%)	V_{oc} (mV)	FF (%)	J_{sc} (mA cm^{-2})	E_g (eV)	J_0 (A cm^{-2})	n	R_{sh} (Ω cm^{-2})	R_s (Ω cm^{-2})	Ref.
Cd, Ag	Li	10.6	663	66.9	23.8	1.46	6.4×10^{-8}	2.13	763	3.90	This work
Cd, Ag	w/o	10.1	650	66.2	23.4	1.45	2.0×10^{-8}	1.88	1600	1.24	39
Ag	K	8.24	670	57.2	21.5	1.54	n/a	n/a	n/a	n/a	40
Cd	Na	9.40	649	63.5	22.8	1.47	7.3×10^{-8}	n/a	n/a	n/a	41
Cd	w/o	12.3	668	67.0	27.0	1.38	3.1×10^{-7}	1.89	n/a	16.6	26
Ge	w/o	10.7	800	63.0	21.0	1.54	n/a	n/a	n/a	n/a	42
Ge	w/o	10.3	757	62.0	21.6	1.58	7.0×10^{-7}	n/a	450	0.34	43
w/o	w/o	11.8	784	69.0	21.7	1.53	2.5×10^{-7}	1.55	n/a	n/a	12
w/o	Na	8.36	700	57.2	20.9	1.61	7.6×10^{-8}	2.27	839	7.67	44

reported for selenium-free CZTS solar cells. This performance results from a balanced combination of V_{oc} (663 mV) and J_{sc} (23.8 mA cm^{-2}), and FF, rather than from the optimization of a single device parameter. When compared with the Cd + Ag (without Li) device reported in Hadke *et al.*,[39] which exhibits slightly lower series resistance and higher shunt resistance, the similar overall efficiencies should not be interpreted as evidence of inferior interface quality in the present work. Instead, the two devices operate under distinct recombination–transport regimes. In our case, Li incorporation predominantly targets grain-boundary and bulk defect passivation, as reflected by the reduced saturation current density ($J_0 = 6.46 \times 10^{-8}$ A cm^{-2}) and moderated ideality factor ($n = 2.13$), both of which are sensitive indicators of non-radiative recombination pathways. These improvements translate directly into enhanced carrier collection and fill factor, even though the open-circuit voltage remains partially limited by residual band-tail states and interface recombination that are intrinsic challenges for pure-sulfide CZTS absorbers. For context, state-of-the-art CZTSSe solar cells fabricated using solution-based processing generally achieve higher efficiencies than sulfide-only CZTS devices, primarily due to the reduced bandgap, improved defect tolerance, and more favorable interface energetics enabled by selenium incorporation. However, when comparisons are restricted to selenium-free, solution-processed CZTS absorbers, the champion efficiency of 10.6% achieved in this work ranks among the highest values reported to date. This comparison highlights that the remaining performance gap relative to CZTSSe devices reflects intrinsic material limitations of sulfide CZTS rather than shortcomings in the processing strategy or device architecture employed here.

By contrast, the higher V_{oc} reported in Hadke *et al.*[39] likely reflects more favorable interface energetics, whereas the present work demonstrates that Li-assisted defect passivation can compensate for non-ideal interfaces by suppressing bulk recombination and improving transport, resulting in comparable overall efficiency. Within this context, the diode parameters of the champion Li:ACZCTS device capture the essential recombination physics relevant to the proposed strategy. A full diode-parameter analysis across all intermediate compositions would not alter this conclusion, as the key contribution of Li is to reduce recombination losses rather than to fundamentally redefine interface energetics. Collectively, these results demonstrate that defect-targeted alloying and alkali-assisted passivation provide an effective pathway to overcome intrinsic recombination losses in sulfide-only CZTS, even in the absence of selenium. This compositional design therefore offers a scientifically robust route toward efficient, selenium-free, and environmentally benign kesterite thin-film photovoltaic devices.

Conclusions

By systematically decoupling the effects of solvents, Cd substitution, Ag alloying, and Li doping, this work establishes a mechanistic framework connecting precursor chemistry, defect suppression, and electronic improvements. Importantly, this study demonstrates that the concurrent integration of Ag–Cd alloying with Li doping in a pure-sulfide CZTS system provides complementary control over bulk, grain-boundary, and interface-related recombination pathways, which has not been previously achieved in sulfide kesterite absorbers. This study addresses critical efficiency limitations in kesterite photovoltaics by demonstrating how solvent engineering combined with Ag–Li co-doping in CZCTS achieves a PCE of 10.6%, representing a substantial improvement compared to the baseline. The systematic investigation based on a solution-processed approach delivers three critical advances for kesterite thin-film technologies: (1) Ag alloying suppresses the persistent Cu–Zn disorder problem, (2) Li doping synergistically enhances hole concentration while passivating grain boundaries, and (3) phase purity is maintained across the doping range, confirmed by Raman analysis. The champion device exhibits a V_{oc} of 663 mV, J_{sc} of 23.86 mA cm^{-2}, and FF of 66.9%, placing it among the most efficient solution-processed kesterite devices to date. While the V_{oc} remains ~564 mV below the Shockley–Queisser limit for a 1.45 eV bandgap, the defect suppression strategies implemented here mark clear progress toward overcoming fundamental material limitations. Notably, the low-temperature, air-stable $LiClO_4$ doping method offers a promising industrially relevant pathway. These results firmly establish Ag–Li co-alloying as a viable and tunable platform for

overcoming intrinsic limitations in kesterite absorber layers. Future work should prioritize interfacial band alignment, surface passivation, and advanced junction design to push efficiencies beyond 12–15%, bringing earth-abundant photovoltaics closer to commercial viability.

Author contributions

O. El Khouja: writing – original draft, writing – review & editing, visualization, validation, methodology, investigation, data curation, conceptualization. Y. Gong: writing – original draft, writing – review & editing, resources, methodology, investigation, conceptualization. A. Jimenez-Arguijo: writing – review & editing, methodology, investigation, conceptualization. I. Assahsahi: writing – review & editing, validation. I. Caño: writing – review & editing, validation. H. Goniotakis: investigation, writing – review & editing, validation. O. Segura-Blanch: writing – review & editing, validation. A. Navarro Güell: writing – review & editing, validation. C. Radu: writing – review & editing, validation, investigation. L. Calvo-Barrio: investigation, validation. S. Giraldo: writing – review & editing, validation, investigation. M. Placidi: writing – review & editing, validation, resources, investigation. Z. Jehl Li-Kao: writing – review & editing, validation, resources. A. C. Galca: writing – review & editing, validation, resources, supervision, funding acquisition. E. Saucedo: writing – review & editing, validation, resources, supervision, funding acquisition.

Conflicts of interest

There are no conflicts to declare.

Data availability

The authors confirm that the data supporting the findings of this study are available within the article or its supplementary information (SI). Supplementary information is available. See DOI: https://doi.org/10.1039/d5ta07702h.

Acknowledgements

NIMP authors acknowledge funding from Ministerul Cercetării, Inovării și Digitalizării (Romanian Ministry of Research, Innovation and Digitalization) through the Core Programme PC3-PN23080303 project, and from Unitatea Executivă pentru Finanțarea Învățământului Superior, a Cercetării, Dezvoltării și Inovării (UEFISCDI) through PN–III–P4-ID-PCE-2020-0827 (contract no. PCE74 09/02/2021) and ERANET-M-3-ERANET-Ligthcell (contract no. 19/15.03.2024) projects. Authors acknowledge the COST Action Research and International Networking project "Emerging Inorganic Chalcogenides for Photovoltaics (RENEW-PV)," CA21148, supported by COST (European Cooperation in Science and Technology). This work also received funding from the European Union's Horizon 2020 research and innovation programme under grant agreement number 101169056 (MENTOR) and 866018 (SENSATE), and by the Science Ministry of Spain (Ministerio de Ciencia, Innovación y Universidades) projects number PID2023-148976OB-C41 and C44 (CURIO-CITY) and PCI2023-145971-2 (CT-FAST). Y.G. thanks the European Union's Horizon research and innovation programme under the Marie Skłodowska-Curie grant agreement no. 101151487 (LEKPV). E.S. is grateful to ICREA (Institució Catalana de Recerca i Estudis Avançats) Academia program. ZJ acknowledges the RyC program (RYC2021-033239-I).

Notes and references

1 S. Giraldo, Z. Jehl, M. Placidi, V. Izquierdo-Roca, A. Pérez-Rodríguez and E. Saucedo, *Adv. Mater.*, 2019, **31**, 1806692.
2 C. Yan, J. Huang, K. Sun, S. Johnston, Y. Zhang, H. Sun, A. Pu, M. He, F. Liu, K. Eder, L. Yang, J. M. Cairney, N. J. Ekins-Daukes, Z. Hameiri, J. A. Stride, S. Chen, M. A. Green and X. Hao, *Nat. Energy*, 2018, **3**, 764–772.
3 Y. Gong, Q. Zhu, B. Li, S. Wang, B. Duan, L. Lou, C. Xiang, E. Jedlicka, R. Giridharagopal, Y. Zhou, Q. Dai, W. Yan, S. Chen, Q. Meng and H. Xin, *Nat. Energy*, 2022, **7**, 966–977.
4 Y. Gong, A. Jimenez-Arguijo, I. Caño, R. Scaffidi, C. Malerba, M. Valentini, D. Payno, A. Navarro-Güell, O. Segura-Blanch, D. Flandre, B. Vermang, A. Perez-Rodriguez, S. Giraldo, M. Placidi, Z. Jehl Li-Kao and E. Saucedo, *Sol. RRL*, 2025, **9**, 2400756.
5 H. Dong, X. Pan, Y. Gong, M. Xue, P. Wang, S. Ho-Kimura, Y. Yao, H. Xin, W. Luo and Z. Zou, *Nat. Commun.*, 2023, **14**, 7969.
6 A. Jimenez-Arguijo, Y. Gong, I. Caño, O. El Khouja, J. Li, K. Sun, Z. Jehl Li-Kao, S. Giraldo, H. Xin, A. Perez-Rodriguez, X. Hao and E. Saucedo, *Nat. Energy*, DOI: 10.1038/s41560-025-01900-y.
7 Y. Gong, Y. Zhang, Q. Zhu, Y. Zhou, R. Qiu, C. Niu, W. Yan, W. Huang and H. Xin, *Energy Environ. Sci.*, 2021, **14**, 2369–2380.
8 Y. Gong, R. Qiu, C. Niu, J. Fu, E. Jedlicka, R. Giridharagopal, Q. Zhu, Y. Zhou, W. Yan, S. Yu, J. Jiang, S. Wu, D. S. Ginger, W. Huang and H. Xin, *Adv. Funct. Mater.*, 2021, **31**, 2101927.
9 J. Shi, J. Wang, F. Meng, J. Zhou, X. Xu, K. Yin, L. Lou, M. Jiao, B. Zhang, H. Wu, Y. Luo, D. Li and Q. Meng, *Nat. Energy*, 2024, **9**, 1095–1104.
10 J. Zhou, X. Xu, H. Wu, J. Wang, L. Lou, K. Yin, Y. Gong, J. Shi, Y. Luo, D. Li, H. Xin and Q. Meng, *Nat. Energy*, 2023, **8**, 526–535.
11 G. Yao, Z. Wu, D. Kou, B. Kong, H. Wei, Z. Shao, W. Zhou, Z. Zhou, S. Yuan, Y. Qi, L. Han, G. Cui and S. Wu, *ACS Energy Lett.*, 2025, 2761–2769.
12 A. Wang, J. Cong, S. Zhou, J. Huang, J. Cao, X. Cui, X. Yuan, Y. Yao, Z. Xu, G. He, J. Z. Liu, J. M. Cairney, Y. Chen, M. A. Green, S.-H. Wei, K. Sun and X. Hao, *Nat. Energy*, 2025, 1–11.
13 T. Wu, S. Chen, Z. Su, Z. Wang, P. Luo, Z. Zheng, J. Luo, H. Ma, X. Zhang and G. Liang, *Nat. Energy*, 2025, **10**, 630–640.
14 R. Fonoll-Rubio, J. Andrade-Arvizu, J. Blanco-Portals, I. Becerril-Romero, M. Guc, E. Saucedo, F. Peiró, L. Calvo-Barrio, M. Ritzer, C. S. Schnohr, M. Placidi, S. Estradé,

V. Izquierdo-Roca and A. Pérez-Rodríguez, *Energy Environ. Sci.*, 2021, **14**, 507–523.
15 S. Kim, J.-S. Park and A. Walsh, *ACS Energy Lett.*, 2018, **3**, 496–500.
16 T. Gokmen, O. Gunawan, T. K. Todorov and D. B. Mitzi, *Appl. Phys. Lett.*, 2013, **103**, 103506.
17 J. Li, Y. Huang, J. Huang, G. Liang, Y. Zhang, G. Rey, F. Guo, Z. Su, H. Zhu, L. Cai, K. Sun, Y. Sun, F. Liu, S. Chen, X. Hao, Y. Mai and M. A. Green, *Adv. Mater.*, 2020, **32**, 2005268.
18 Y. Gong, Y. Zhang, E. Jedlicka, R. Giridharagopal, J. A. Clark, W. Yan, C. Niu, R. Qiu, J. Jiang, S. Yu, S. Wu, H. W. Hillhouse, D. S. Ginger, W. Huang and H. Xin, *Sci. China Mater.*, 2021, **64**, 52–60.
19 Y. Gong, H. Xin and L. Ding, *J. Semicond.*, 2021, **42**, 100201.
20 G. Larramona, S. Levcenko, S. Bourdais, A. Jacob, C. Choné, B. Delatouche, C. Moisan, J. Just, T. Unold and G. Dennler, *Adv. Energy Mater.*, 2015, **5**, 1501404.
21 C. Niu, Y. Gong, R. Qiu, Q. Zhu, Y. Zhou, S. Hao, W. Yan, W. Huang and H. Xin, *J. Mater. Chem. A*, 2021, **9**, 12981–12987.
22 Y. Cui, M. Wang, P. Dong, S. Zhang, J. Fu, L. Fan, C. Zhao, S. Wu and Z. Zheng, *Advanced Science*, 2022, **9**, 2201241.
23 Y. Qi, Q. Tian, Y. Meng, D. Kou, Z. Zhou, W. Zhou and S. Wu, *ACS Appl. Mater. Interfaces*, 2017, **9**, 21243–21250.
24 J. Fu, D. Kou, W. Zhou, Z. Zhou, S. Yuan, Y. Qi and S. Wu, *J. Mater. Chem. A*, 2020, **8**, 22292–22301.
25 T. Todorov, H. W. Hillhouse, S. Aazou, Z. Sekkat, O. Vigil-Galán, S. D. Deshmukh, R. Agrawal, S. Bourdais, M. Valdés, P. Arnou, D. B. Mitzi and P. J. Dale, *J. Phys.: Energy*, 2020, **2**, 012003.
26 X. Pan, X. Li, Y. Yang, C. Xiang, A. Xu, H. Liu, W. Yan, W. Huang and H. Xin, *Adv. Energy Mater.*, 2023, **13**, 2301780.
27 Y. E. Romanyuk, S. G. Haass, S. Giraldo, M. Placidi, D. Tiwari, D. J. Fermin, X. Hao, H. Xin, T. Schnabel, M. Kauk-Kuusik, P. Pistor, S. Lie and L. H. Wong, *J. Phys.: Energy*, 2019, **1**, 044004.
28 O. El Khouja, C. C. Negrila, K. Nouneh, M. Secu, M. Ebn Touhami, E. Matei, V. Stancu, M. Enculescu, V. Kuncser and A. C. Galca, *J. Alloys Compd.*, 2022, **906**, 164379.
29 Z. Su, J. M. R. Tan, X. Li, X. Zeng, S. K. Batabyal and L. H. Wong, *Adv. Energy Mater.*, 2015, **5**, 1500682.
30 Z. Su, G. Liang, P. Fan, J. Luo, Z. Zheng, Z. Xie, W. Wang, S. Chen, J. Hu, Y. Wei, C. Yan, J. Huang, X. Hao and F. Liu, *Adv. Mater.*, 2020, **32**, 2000121.
31 O. El Khouja, Y. Gong, A. Jimenez-Arguijo, M. J. Guerra, A. G. Medaille, R. Scaffidi, A. Basak, C. Radu, D. Flandre, B. Vermang, S. Giraldo, M. Placidi, Z. J. Li-Kao, A. C. Galca and E. Saucedo, *Prog. Photovolt.: Res. Appl.*, 2025, **33**, 628–643.
32 Y. Gong, A. Jimenez-Arguijo, A. G. Medaille, S. Moser, A. Basak, R. Scaffidi, R. Carron, D. Flandre, B. Vermang, S. Giraldo, H. Xin, A. Perez-Rodriguez and E. Saucedo, *Adv. Funct. Mater.*, 2024, **34**, 2404669.
33 X. Zhong, J. Wang, L. Han, J. Chi, T. Liu, D. Kou, W. Zhou, Z. Zhou, S. Yuan, Y. Meng, Y. Qi, Q. Meng and S. Wu, *Adv. Funct. Mater.*, 2025, **35**, 2418548.
34 H. Zhou, W.-C. Hsu, H.-S. Duan, B. Bob, W. Yang, T.-B. Song, C.-J. Hsu and Y. Yang, *Energy Environ. Sci.*, 2013, **6**, 2822.
35 D. Dumcenco and Y.-S. Huang, *Opt. Mater.*, 2013, **35**, 419–425.
36 M. Dimitrievska, A. Fairbrother, X. Fontané, T. Jawhari, V. Izquierdo-Roca, E. Saucedo and A. Pérez-Rodríguez, *Appl. Phys. Lett.*, 2014, **104**, 021901.
37 M. He, X. Zhang, J. Huang, J. Li, C. Yan, J. Kim, Y.-S. Chen, L. Yang, J. M. Cairney, Y. Zhang, S. Chen, J. Kim, M. A. Green and X. Hao, *Adv. Energy Mater.*, 2021, **11**, 2003783.
38 D. Abou-Ras, S. Weitz, J. Huang, K. Sun, Y. Gong, A. Jimenez-Arguijo, M. Dimitrievska, X. Hao and E. Saucedo, *Energy Environ. Mater.*, 2025, e70048.
39 S. H. Hadke, S. Levcenko, S. Lie, C. J. Hages, J. A. Márquez, T. Unold and L. H. Wong, *Adv. Energy Mater.*, 2018, **8**, 1802540.
40 A. Ibrahim, A. Guchhait, S. Hadke, H. L. Seng and L. H. Wong, *ACS Appl. Energy Mater.*, 2020, **3**, 10402–10407.
41 H. Sun, J. Huang, A. O'Neill, J. S. Yun, T. L. Young, C. Yan, K. Sun, J. Li, M. P. Nielsen, X. Cui, A. Wang, J. Seidel, J. A. Stride, M. A. Green and X. Hao, *Sol. RRL*, 2022, **6**, 2200442.
42 A. Wang, J. Huang, J. Cong, X. Yuan, M. He, J. Li, C. Yan, X. Cui, N. Song, S. Zhou, M. A. Green, K. Sun and X. Hao, *Adv. Mater.*, 2024, **36**, 2307733.
43 X. Yuan, J. Li, J. Huang, C. Yan, X. Cui, K. Sun, J. Cong, M. He, A. Wang, G. He, A. Mahboubi Soufiani, J. Jiang, S. Zhou, J. A. Stride, B. Hoex, M. Green and X. Hao, *Small*, 2022, **18**, 2204392.
44 H. Liu, Y. Li, A. Xu, X. Li, C. Xiang, S. Zhou, S. Wang, W. Yan and H. Xin, *Sol. RRL*, 2024, 2400588.